(Received 17 April 2026, Accepted 18 May 2026, Scheduled 9 June 2026)

Research on the Performance of Permanent Magnet Synchronous Motors with Optimized Stator-Rotor and Hybrid Permanent Magnet Structure

Han Lin, Huawei Liu*, and Zhonggen Wang

School of Electrical and Information Engineering, Anhui University of Science and Technology, Huainan 232001, China

ABSTRACT: To address the trade-off between increasing output torque and reducing torque ripple and cogging torque in interior permanent magnet synchronous motors (IPMSMs), this study proposes a structure incorporating stator-rotor auxiliary slots and rotor damping holes. Additionally, a hybrid permanent magnet configuration combining N35 and N30 grades was adopted to maintain high performance while further reducing costs. First, an analytical expression for the cogging torque was derived, and a finite element model of the motor was established. Subsequently, a parametric sweep and optimization of the stator and rotor auxiliary slots were conducted to obtain the optimal combination of auxiliary slot dimensions. Furthermore, a multi-objective optimization algorithm was proposed to optimize the motor parameters. Finally, radial electromagnetic force analysis was performed on the optimized motor model. The results demonstrate that the proposed structure effectively suppresses the torque ripple, cogging torque, and amplitude of the radial electromagnetic force, thereby reducing motor vibration amplitude while ensuring that the electromagnetic torque remains unaffected. The proposed design achieves a favorable balance between output torque enhancement and torque ripple/cogging torque reduction, with cost control through hybrid permanent magnets, demonstrating comprehensive performance improvements for IPMSMs.

1. INTRODUCTION

Permanent magnet synchronous motors (PMSMs), known for their high power density and high efficiency, were recognized as the core actuators for electric vehicle drive systems [1, 2]. Driven by the continuous development of the new energy vehicle industry, interior permanent magnet synchronous motors (IPMSMs), with their longer service life and superior overall performance [3, 4], gradually became the mainstream direction of technological evolution in this field. Meanwhile, the industrial application of hairpin winding technology accelerated [5, 6], which not only significantly expanded the power density limit of motors but also profoundly reshaped their thermal management design paradigm.

Studies in [7–9] have shown that, compared with the traditional single-layer magnet structure, a dual-layer magnet rotor structure can significantly improve the saliency ratio of the motor, thereby enhancing its flux-weakening and speed expansion capability, allowing the motor to maintain high efficiency over a wider speed range. Based on existing research, further comparison of different interior rotor topologies reveals that, compared with the traditional V-type interior permanent magnet arrangement, the VV-type interior rotor structure can further optimize the flux path and form a multi-layer flux barrier synergistic effect [10, 11]. Specifically, the VV-type structure significantly improved the saliency ratio and reluctance torque utilization of the motor by adding an additional layer of V-shaped magnets, thereby enabling the motor to maintain high efficiency over a wider flux-weakening speed range. Meanwhile, due to the staggered arrangement of the two-layer magnets, which effectively weakened the harmonic coupling between stator slots and rotor poles, the cogging torque and torque ripple were further suppressed. In addition, the VV-type topology helped to disperse the concentration of the demagnetizing field at the magnet ends. Combined with an appropriate selection of permanent magnet materials, the overall demagnetization resistance of the motor was significantly enhanced [12], improving operational reliability under complex working conditions. Therefore, the VV-type interior rotor structure exhibited comprehensive advantages over the traditional V-type structure in achieving high torque density, low vibration and noise, and strong flux-weakening speed expansion capability. Meanwhile, by optimizing the rotor topology and adjusting the magnetization pattern of the magnets, the cogging torque and torque ripple were effectively reduced, thereby improving the running smoothness of the motor. In addition, the reasonable selection of permanent magnet materials was also identified as an important means to improve motor performance, which could significantly enhance the demagnetization resistance of the motor and ensure its reliability under complex operating conditions.

It is stated in [13] that because the permanent magnets (PMs) in the rotor section were subjected to high temperatures during motor operation, the arrangement of magnetic bridges should be considered in rotor structure design to reduce the risk of irreversible demagnetization of the PMs. Studies in [14, 15] show that setting auxiliary slots on the stator or rotor core can ef-

* Corresponding author: Huawei Liu (19155451194@163.com).

fectively weaken the harmonic components in the air-gap magnetic field, thereby significantly reducing the cogging torque and improving the control accuracy and operational stability of the motor. Ref. [16] proposed a motor structure adopting hybrid PMs by combining ferrite and neodymium iron boron (NdFeB), which effectively reduced the manufacturing cost of the motor while maintaining the required output performance. Ref. [17] used the response surface method to optimize a hybrid permanent magnet motor in order to minimize the amount of permanent magnet material while achieving the required torque rating. Ref. [18] performed a multi-objective optimization based on an analytical model and the particle swarm optimization (PSO) algorithm, which improved the torque performance of the hybrid permanent magnet motor and reduced the magnet cost. Refs. [19, 20] introduced a sensitivity analysis method combined with a hierarchical optimization strategy, which greatly reduced the computation time in the multi-parameter optimization process and improved the design efficiency. Refs. [21, 22] used output torque, cogging torque, and torque ripple as objectives and optimized the key structural parameters of the motor using a multi-objective genetic algorithm, finally obtaining a set of design schemes with optimal comprehensive performance. From the perspective of vibration and noise, Refs. [23–25] systematically investigated the vibration response mechanism of a motor during operation by analyzing the radial electromagnetic force and modal characteristics. Ref. [26] adopted the Halbach magnetization technology to reduce cogging torque and torque ripple to improve the overall performance of the motor.

This study addresses the technical bottleneck of increased cogging torque caused by the addition of damping holes in traditional rotor structures, where a single structural optimization method can hardly simultaneously achieve torque improvement while suppressing torque ripple and cogging torque. A novel rotor structure is proposed that balances electromagnetic performance improvement with cogging torque suppression. Through the hybrid configuration of different grades of NdFeB permanent magnets, the effective control of material cost is achieved, thereby overcoming the drawback that damping holes increase torque but also raise cogging torque. Finally, Halbach magnetization technology is employed to further enhance the motor performance. First, the fundamental electromagnetic performance of the motor was systematically analyzed, and a high-fidelity finite element simulation model was established. Second, on the basis of reasonably arranging damping holes in the rotor, auxiliary slots were further introduced into the stator and rotor cores. The radii of the auxiliary slots were optimized using a parametric sweep method, so that various performance indicators were synergistically improved to a satisfactory level. Third, a hierarchical collaborative optimization strategy was introduced to systematically optimize the topological structural parameters, further exploiting the comprehensive performance potential of the structure. On this basis, a hybrid arrangement of N30 and N35 NdFeB permanent magnets was adopted to construct four typical combination configurations. Through refined adjustment of their geometric parameters and spatial arrangement, the optimal permanent magnet combination scheme was determined. Subsequently, by comparing the radial air-gap flux density and radial electromagnetic force of the motor before and after optimization, the effectiveness and robustness of the proposed structure in terms of electromagnetic performance and vibration suppression were systematically verified. Finally, a Halbach segmented magnetization method was introduced for the second-layer permanent magnets. Through joint regulation of the magnetization length and angle, a further leap in electromagnetic performance was achieved. Overall, the multi-method collaborative optimization path proposed in this paper fully integrated multidimensional approaches, such as structural topology, magnetic circuit design, and magnetization strategy, providing a new systematic solution for the design of permanent magnet motors with high cost-effectiveness and low cogging torque.

2. MOTOR STRUCTURAL DESIGN

2.1. IPMSM Topology and Key Performance Indicators

Currently, interior permanent magnet synchronous motors are widely used as drive motors in the electric vehicle sector. Their magnet layout has evolved from single-layer designs to predominantly adopting double-layer VV-type structures, which were favored for their excellent electromagnetic performance.

In this study, a two-dimensional electromagnetic field finite element model of a "VV"-type rotor interior permanent magnet synchronous motor was constructed using Maxwell finite element simulation software, as shown in Fig. 1. To ensure the standardization and reproducibility of the research, this study defines the key design parameters of the motor, specifically the stator and rotor structure dimensions, permanent magnet parameters, and winding configuration. The core initial values are listed in Table 1. In subsequent comparative studies on different rotor topologies, to strictly control the variables and ensure the scientific validity and comparability of the research results, this study adheres to the fundamental principles of the control variable method. It is explicitly stipulated that, apart from the rotor structure itself, all other basic motor parameters will remain strictly consistent with those listed in Table 1.

TABLE 1. Motor basic parameters.

Parameter Name	Parameter Value
Stator Outer Diameter (mm)	200
Stator Inner Diameter (mm)	164
Rotor Outer Diameter (mm)	162.6
Rotor Inner Diameter (mm)	80
Rated Speed (r/min)	12000
Air Gap Length (mm)	0.7
Number of Pole Pairs	4
Number of Slots	48
Core Length (mm)	200
Rated Power (kW)	117
Rated Voltage (V)	220
Rated Torque (N·m)	93.11

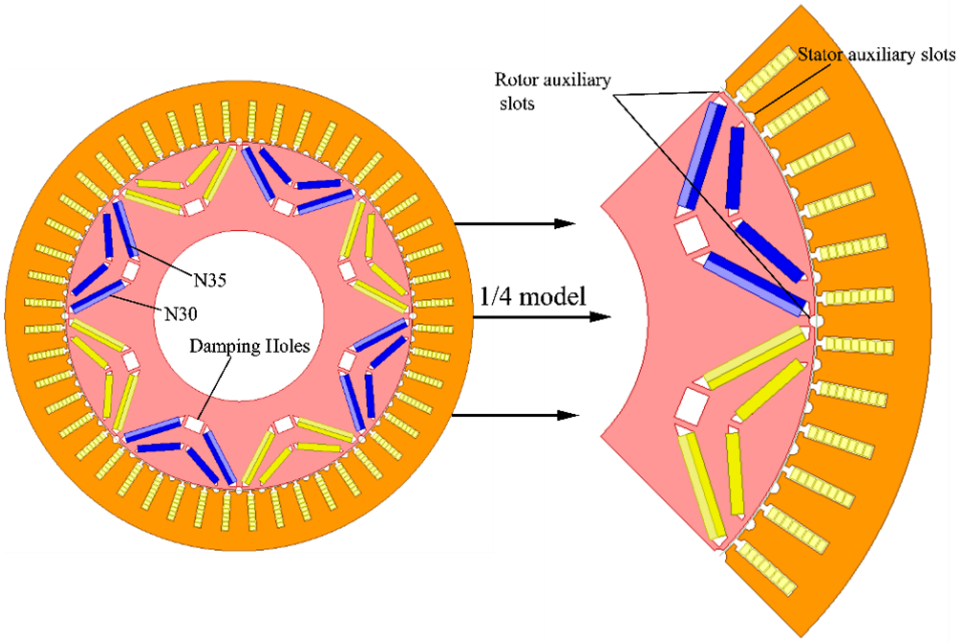

FIGURE 1. Motor structure.

2.2. Theoretical Analysis of Motor Cogging Torque and Vibration

In the d-q rotating reference frame, after a series of derivations and transformations, the voltage equations of the PMSM can be expressed as:

$$u_d = R_s i_d + L_d \frac{di_d}{dt} - w_e L_q i_q \tag{1}$$

$$u_q = R_s i_q + L_q \frac{di_d}{dt} + w_e L_d i_d + \omega_e \psi_f \tag{2}$$

where u_d and u_q are the d-axis and q-axis stator voltages, respectively; i_d and i_q are the d-axis and q-axis stator currents, respectively; R_s is the stator phase resistance; and ω_e is the electrical angular velocity.

$$\begin{cases} \psi_d = L_d i_d + \psi_f \\ \psi_q = L_q i_q \end{cases} \tag{3}$$

where ψ_d and ψ_q are the d-axis and q-axis flux linkages, respectively; L_d and L_q are the d-axis and q-axis inductances, respectively; and ψ_f is the excitation flux linkage generated by the permanent magnets.

The electromagnetic torque equation is given as follows:

$$\begin{cases} T_m = \dfrac{3}{2} P \psi_f i_q \\ T_r = \dfrac{3}{2} P (L_d - L_q) i_q i_q \end{cases} \tag{4}$$

$$T_e = T_m + T_{r=} \frac{3}{2} P [\psi_f i_q + (L_d - L_q) i_q i_q] \tag{5}$$

where T_e is the electromagnetic torque, T_m the permanent magnet torque, T_r the reluctance torque, and P the number of poles.

This equation indicates that the electromagnetic torque consists of two components: permanent magnet torque and reluctance torque.

The expression for the cogging torque of the motor is given by:

$$T_{cog} = -\frac{\partial W}{\partial \alpha} \tag{6}$$

where W represents the magnetic field energy stored in the air gap.

As a result of the air-gap magnetic field harmonics, the motor generates electromagnetic force waves of different frequencies and orders. By separately analyzing the stator-rotor magnetomotive force (MMF) and the air-gap permeance, the expression for the air-gap flux density can be derived as follows:

$$B_r(\theta, t) = f_a(\theta, t) \Lambda(\theta, t) \tag{7}$$

where θ represents the Halbach magnetization angle of the permanent magnets. According to the method of magnetomotive force (MMF) multiplied by permeance, the radial air-gap flux density $B_r(\theta, t)$ can be expressed as the product of the air-gap MMF $f_a(\theta, t)$ and relative air-gap permeance function $\Lambda(\theta, t)$.

The radial and tangential electromagnetic force amplitudes F_r and F_t of the motor are expressed as follows:

$$\begin{cases} F_r = \dfrac{B_r^2 - B_t^2}{2\mu_0} \approx \dfrac{B_r^2}{2\mu_0} \\ F_t = \dfrac{B_r^2 B_t^2}{2\mu_0} \end{cases} \tag{8}$$

where B_r^2 and B_t^2 are the radial and tangential components of the air-gap flux density at the stator teeth, respectively, and μ_0 is the vacuum permeability.

TABLE 2. Comparison of motor performance parameters with and without damping holes.

Performance Parameters	With Damping Holes	Without Damping Holes
Average Torque (N·m)	107.27	93.11
Torque Ripple (%)	11.36	13.22
Peak Back-EMF (V)	242.95	216.43
Cogging Torque (mN·m)	399.21	286.85
Back-EMF THD (%)	3.22	3.24

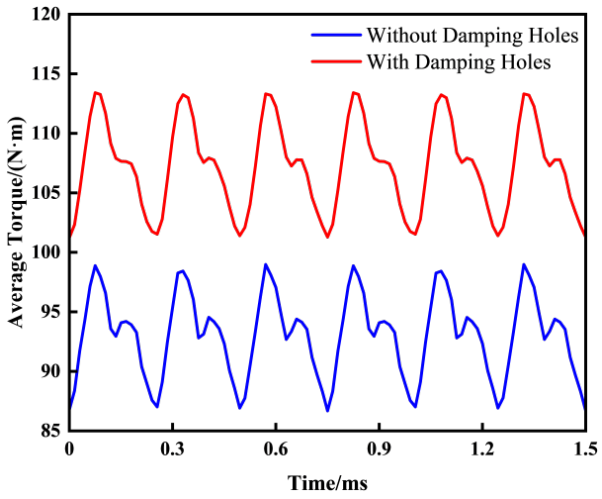

FIGURE 2. Average torque comparison curve of the motor.

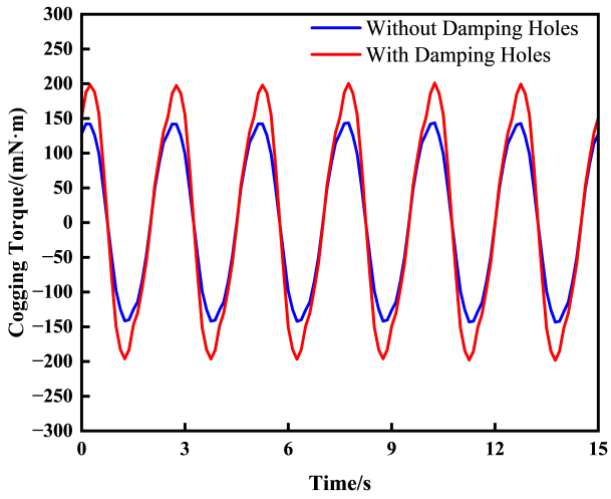

FIGURE 3. Cogging torque comparison curve.

The specific mathematical expression for the radial electromagnetic force, $F_r(\theta, t)$, of the motor is given by

$$F_r(\theta,t) = \frac{B_r^2}{2\mu_0} = \frac{[f_r(\theta,t) + f_t(\theta,t)]^2 \Lambda_s^2(\theta)}{2\mu_0} \quad (9)$$

where Λ_s is the stator air-gap permeance.

3. MOTOR STRUCTURAL OPTIMIZATION

This section presents the preliminary optimization of the motor, through which the motor performance is gradually improved using methods such as damping holes, stator and rotor auxiliary slots, and multi-objective optimization. Damping holes are designed to increase the average torque and reduce the torque ripple. The stator and rotor auxiliary slots are designed and optimized through a parametric sweep to suppress cogging torque while maintaining high torque and low torque ripple. Subsequently, multi-objective optimization is employed to further enhance various performance parameters by modifying the motor topology. Finally, based on different combinations of hybrid permanent magnets, four motor configurations were designed and subjected to parametric sweeps, and the optimal combination was selected through comparison. The rotor step-skewing method can significantly suppress torque ripple. Finite element calculations revealed that as the number of segments increased, the average torque continuously decreased, and the optimization effect showed little change after three segments. Finally, this paper adopted a linear step skewing with three equal segments, each with a skew angle of 5°.

3.1. Design of Damping Holes

To compare the motor performance before and after the design of the damping holes, an analysis was conducted based on four aspects: average torque, torque ripple, cogging torque, and back electromotive force (back-EMF). The torque and cogging torque comparison curves of the VV-type IPMSM with and without damping holes are shown in Fig. 2. A comparison of the motor performance parameters is presented in Table 2. After designing the damping holes in the rotor, the output torque of the motor was 107.27 N·m, and the torque ripple was 11.36%. Compared with the VV-type motor without damping holes, the output torque increased by 14.16 N·m, whereas the torque ripple was reduced by 1.86%.

Figure 3 shows the cogging torque comparison curves for the motor with and without damping holes. After the addition of damping holes, the average torque improved, and the torque ripple was suppressed, whereas the cogging torque increased. Therefore, further optimization of the motor structure is required to reduce cogging torque.

Figure 4 shows the back-EMF waveforms and corresponding harmonic analysis results for the VV-type IPMSM with and without damping holes. From Fig. 4(a), it can be observed that the back-EMF waveform of the motor with damping holes is closer to sinusoidal. Fig. 4(b) shows that, after the addition of damping holes, the harmonics of most orders are reduced compared with those of the motor without damping holes, except for the fundamental, 3rd, and 13th harmonics, which are slightly higher. The total harmonic distortion (THD) of the back-EMF

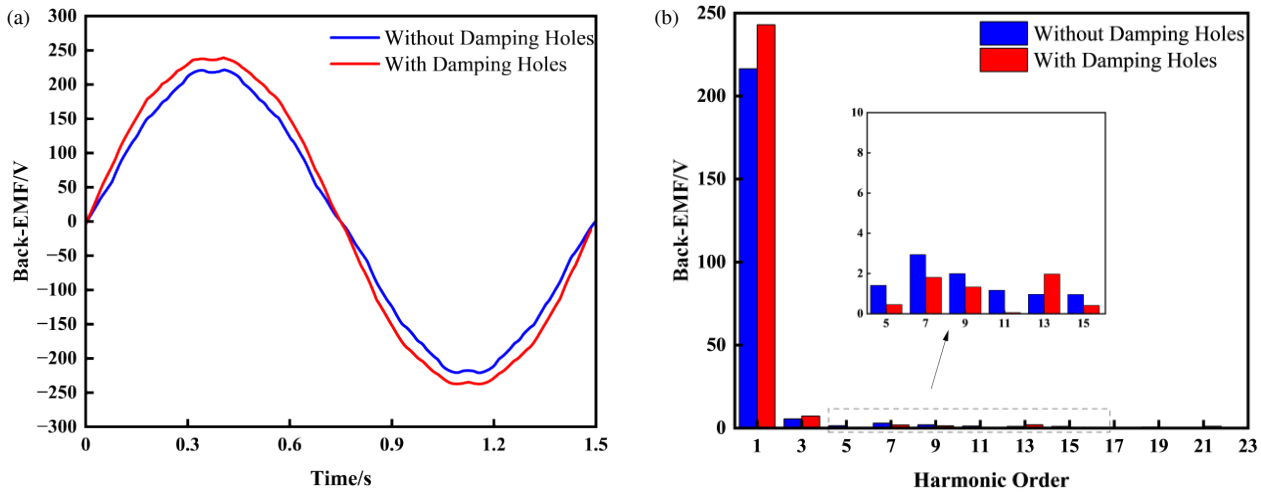

FIGURE 4. Analysis of motor back-EMF and its harmonics: (a) Back-EMF waveform of the motor, (b) Harmonic content of motor Back-EMF.

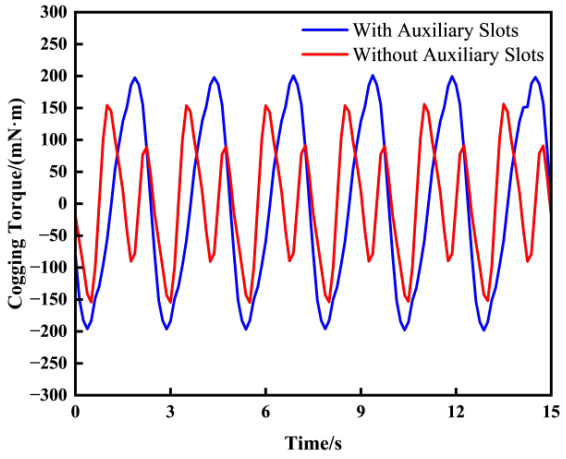

FIGURE 5. Comparison of cogging torque with and without auxiliary slots.

can be expressed as:

$$\text{THD} = \frac{U_{nrms}}{U_{1rms}} \tag{10}$$

where U_{nrms} is the root-mean-square (RMS) value of the harmonics, and U_{1rms} is the RMS value of the fundamental.

Using Equation (12), the back-EMF THD of the motor with damping holes and the motor without damping holes are calculated to be 3.22% and 3.24%, respectively. The back-EMF THD was reduced by 0.02% (from 3.24% to 3.22%).

3.2. Stator and Rotor Auxiliary Slot Design

For interior permanent magnet synchronous motors, the harmonic order of the cogging torque varies with different pole-slot combinations. The harmonic order of the cogging torque, denoted as f_{pn}, can be expressed as:

$$f_{pn} = \frac{kN_L}{2p}, \quad k = 1, 2, 3, \ldots \tag{11}$$

where p is the number of pole pairs of the motor, and N_L is the least common multiple of the number of stator slots and the number of poles.

In the cogging torque of interior permanent magnet synchronous motors, the higher the harmonic order is, the smaller its amplitude is. Therefore, by adjusting the stator and rotor slotting to change the parameter N_L, the cogging torque can be effectively suppressed.

Figure 5 shows a comparison of the cogging torque with and without auxiliary slots on both the stator and rotor. The auxiliary slots significantly weakened the cogging torque, reducing it by 100 mN·m. This indicates that incorporating both auxiliary slots and damping holes can enhance the output torque while suppressing the cogging torque and torque ripple, thereby improving the overall motor performance.

To further reduce the cogging torque while maintaining a high torque level, a parametric sweep was performed for rotor auxiliary slot R_1 and stator auxiliary slot R_2. The response surfaces for the cogging torque, average torque, torque ripple, and core loss are shown in Fig. 6.

As shown in Fig. 6(a), both R_1 and R_2 significantly influence the cogging torque, which exhibits local minima. Fig. 6(b) shows the response surface of R_1 and R_2 with respect to the average torque. It can be seen that the rotor auxiliary slot R_1 has a relatively minor effect on the average torque, whereas the stator auxiliary slot R_2 has a more pronounced impact, with the average torque decreasing as R_2 increases. Fig. 6(c) illustrates the response surface of R_1 and R_2 with respect to the torque ripple. Both parameters influence torque ripple, exerting a suppressive effect, with the torque ripple initially increasing and then decreasing as R_1 increases. Fig. 6(d) shows the response surface of R_1 and R_2 with respect to the core loss, where the influence pattern is similar to that observed for the average torque.

Based on the above response surface curves, when the rotor auxiliary slot $R_1 = 0.2$ mm and stator auxiliary slot $R_2 = 0.8$ mm, the various performance values of the motor can reach a relatively high level: After optimization using stator-rotor auxiliary slots and damping holes, the average torque of the mo-

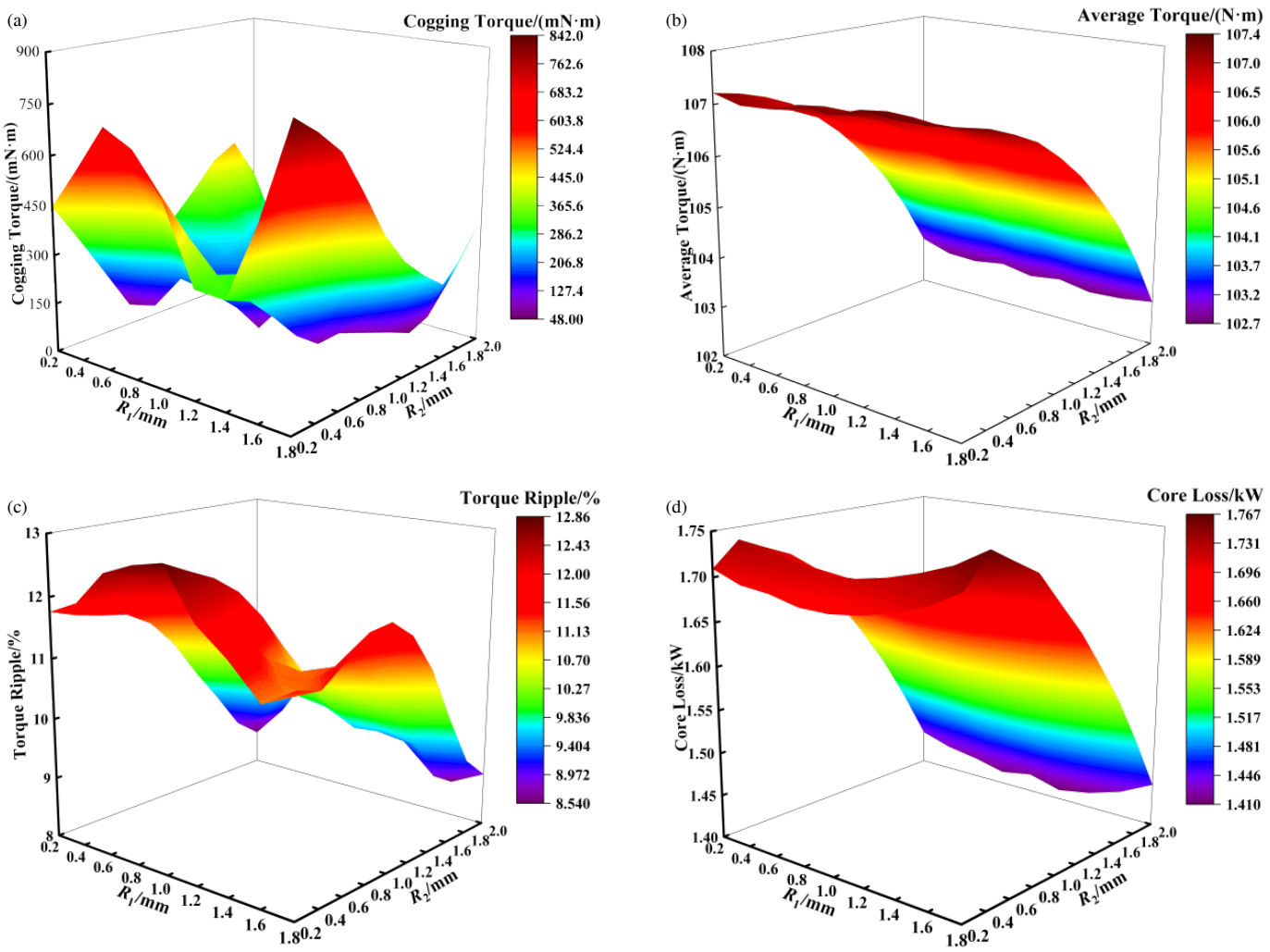

FIGURE 6. Optimization of response surface results: (a) Response surface of cogging torque versus R_1 and R_2, (b) Response surface of average torque versus R_1 and R_2, (c) Response surface of torque ripple versus R_1 and R_2, (d) Response surface of core losses versus R_1 and R_2.

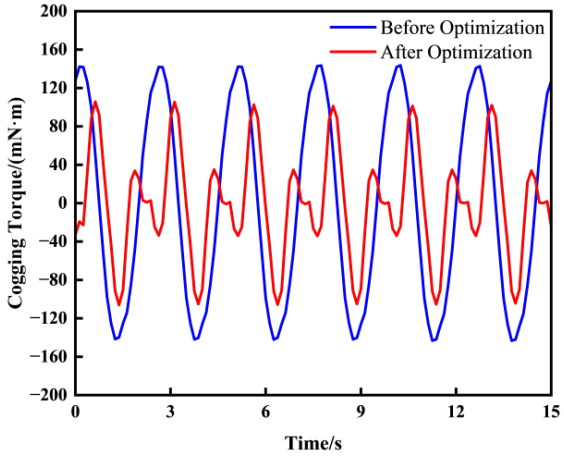

FIGURE 7. Cogging torque waveforms before and after optimization.

tor was 107.71 N·m (an increase of 14.6 N·m), the torque ripple was 11.23% (a reduction of 1.99%), and the core loss was 1.709 kW. As shown in Fig. 7, the optimized cogging torque was 211.96 mN·m, a reduction of 187.25 mN·m.

3.3. Air-Gap Flux Density and Radial Electromagnetic Force Analysis

After designing the damping holes and auxiliary slots, the waveforms of the air-gap flux density and radial electromagnetic force of the motor are shown in Fig. 8. The amplitudes of the radial electromagnetic force and air-gap flux density waveforms were significantly decreased, indicating that the rotor damping holes and stator-rotor auxiliary slot structure can effectively suppress motor vibration.

3.4. Multi-Objective Optimization

During the multi-objective optimization process of the motor, there were usually mutual constraints and coupling relationships among the various optimization objectives: an improvement in one performance indicator often came at the cost of a decline in other performance metrics. Therefore, it was difficult to find a perfect solution where all objectives were simultaneously optimized. To address this, a Pareto front solution set was generally introduced in multi-objective optimization of motors, serving as the set of optimal solutions that achieved a trade-

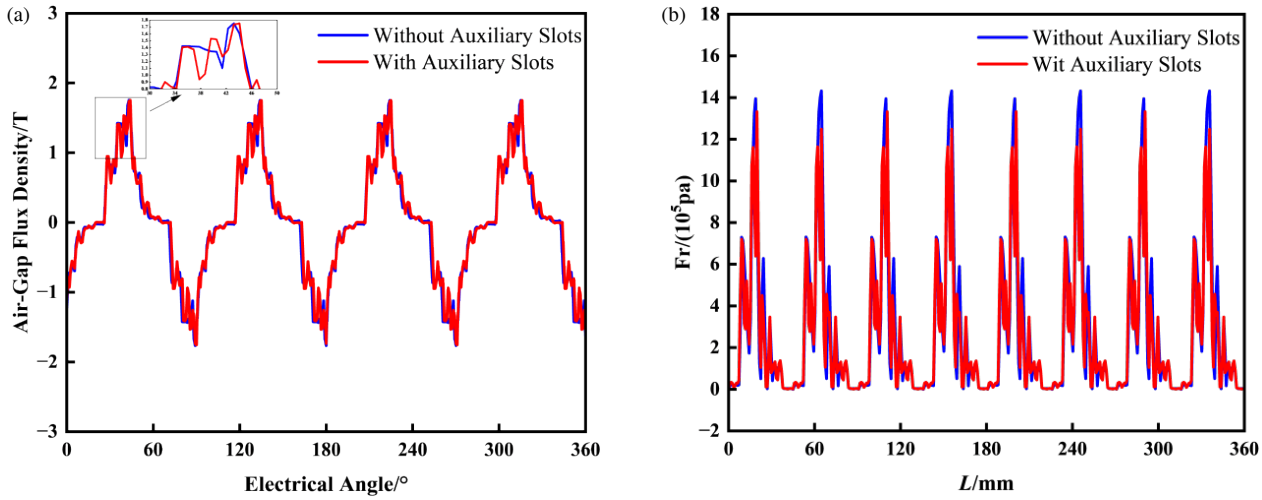

FIGURE 8. Air-gap flux density and electromagnetic force waveforms: (a) Air-Gap flux density spatial distribution waveform, (b) Radial electromagnetic force spatial distribution waveform.

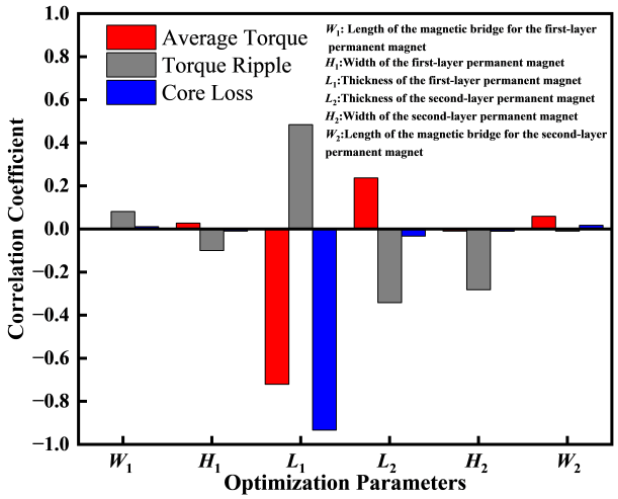

FIGURE 9. Sensitivity analysis.

off among the objectives. The core goal of hierarchical multi-objective optimization was precisely to more finely screen the final design scheme from this Pareto front set. Specifically, after the first level of optimization was completed, three sample points with appropriate spacing from each other were selected from the obtained Pareto front as the initial points for the next level of optimization. After the second level of optimization was completed, three points with reasonable spacing were again selected from the new Pareto front to form the final optimization scheme. To verify the superiority of this hierarchical optimization strategy, the widely used multi-objective evolutionary algorithm was employed in this paper to perform the optimization search.

To improve the computational efficiency of the optimization process, a parameter sensitivity analysis was carried out before the optimization design to quantify the contribution of each design variable to the optimization objectives. Since motor optimization problems usually involve numerous design parameters and performance indicators, the traditional single-parameter scanning method not only imposed a heavy computational burden but also made it difficult to ensure modeling accuracy. Therefore, the correlation coefficient method was introduced in this paper to quantitatively evaluate the parameter sensitivity, and its evaluation index was defined as follows:

$$S(X) = \frac{\sum_{i=1}^{n}(X_i - \bar{X})(Y_i - \bar{Y})}{\sqrt{\sum_{i=1}^{n}(X_i - \bar{X})^2 \sum_{i=1}^{n}(Y_i - \bar{Y})^2}} \tag{12}$$

where n is the number of samples; X_i and Y_i are the rank values of the design parameter and the objective function corresponding to the i sample, respectively; and $\bar{X}$ and $\bar{Y}$ are the average rank values of the design parameter and the objective function, respectively.

As shown in Fig. 9, the parameters L_1, L_2, and H_2 have relatively large influence coefficients on the torque, torque ripple, and core loss. A layered optimization approach is adopted: these three parameters are selected first. After the first round of optimization was completed, a set of parameter solutions with better optimization results was obtained. Then, the remaining parameters were optimized in the second round. The final optimization results are presented in Table 3.

TABLE 3. Comparison of parameters before and after optimization.

Parameter	Initial Value	Optimal Value
W_1 (mm)	3	2.88
H_1 (mm)	4.5	4.67
L_1 (mm)	54	53.05
L_2 (mm)	32	40.07
H_2 (mm)	3.2	3.18
W_2 (mm)	25	20.19
Average Torque (N·m)	107.71	118.25
Torque Ripple (%)	11.23	3.4
Core Loss (kW)	1.709	1.686

After the multi-objective hierarchical optimization, the final optimization results of the motor were as follows: the average torque increased by 11.54 N·m to 118.25 N·m; the torque ripple decreased by 8.03% to 3.4%; and the total loss decreased by 23 W to 1.686 kW. Although cogging torque was not set as an optimization objective in this optimization, it was still reduced by 25.86 mN·m to 185.1 mN·m.

3.5. Analysis of Radial Electromagnetic Force after Multi-Objective Optimization

According to the optimization results, after the combined design of topology optimization, parametric sweep, and multi-objective optimization, the radial electromagnetic force was reduced to a certain extent. A comparison of the radial electromagnetic force waveforms before and after optimization is shown in Fig. 10. As shown in Fig. 10, the amplitude of the radial electromagnetic force of the optimized motor decreased, changing from 1.33 MPa before optimization to 0.98 MPa after optimization. The three-dimensional radial electromagnetic force density waveforms before and after optimization were shown in Fig. 11, which, to some extent, reflected a decreasing trend in both the amplitude and mean value of the radial electromagnetic force after optimization, and this might help suppress the generation of motor vibration and noise at the source.

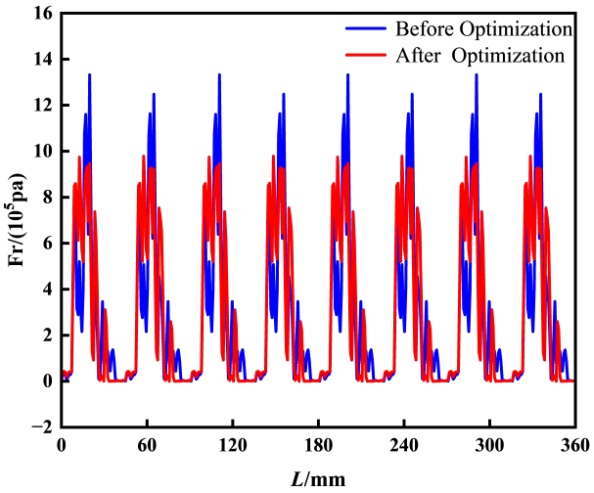

FIGURE 10. Comparison of radial electromagnetic force waveforms before and after optimization.

4. OPTIMIZATION OF HYBRID PERMANENT MAGNETS

NdFeB magnets, the most widely used rare-earth permanent magnet materials, exhibit extremely high energy products. To further reduce the cost of NdFeB magnets, a hybrid permanent magnet configuration combining N30 and N35 grades, which offer lower energy products and lower prices, is adopted. The parameters of the different NdFeB magnet grades are listed in Table 4.

To investigate the influence of different N30 and N35 PM combination schemes on motor performance, four combination configurations are designed in this study, corresponding to Motors A–D, as shown in Figs. 12(a)–(d). L_3 denotes the PM width of the upper half of the second-layer PMs in Motors A and B, with an initial value of 2.31995 mm; L_4 denotes the PM length of the middle section of the second-layer PMs in Motors C and D, with an initial value of 27 mm. Table 5 presents the performance parameters of the four motors under initial conditions.

TABLE 4. Comparison of parameters between N30 and N35.

Parameter	N30	N35
Maximum Energy Product (kJ/m^3)	$223 \sim 255$	$253 \sim 292$
Hcb (kA/m)	$800 \sim 836$	$860 \sim 915$
Hcj (kA/m)	$955 \sim 1035$	$955 \sim 1035$
Cost (RMB/kg)	$155 \sim 165$	$183 \sim 193$

To obtain the optimal PM combination scheme and investigate the effects of L_3 and L_4 on the average torque, torque ripple, and cogging torque of the motor, a parametric sweep of L_3 and L_4 was performed in this study.

Figure 13 shows the influence curves of L_3 on the average torque and torque ripple of Motors A and B. The average torque of Motors A and B exhibited increasing and decreasing trends, respectively. It is worth noting that the torque ripple of both motors presents significant fluctuations; meanwhile, Motor B achieves a low torque ripple while maintaining a high torque output when L_3 is approximately 3.7 mm, which should be considered in the subsequent comparative analysis.

Figure 14 presents the influence curves of L_4 on the average torque and torque ripples of Motors C and D. The variation trends of the average torque for Motors C and D are generally consistent with those of Motors A and B, while the torque ripple of Motor C reaches its minimum value at $L_4 = 37$ mm, which should be the key focus in the subsequent comparative study.

Figure 15 shows the influence curves of L_3 and L_4 on the cogging torque of the four motors (L_3 corresponds to Motors A and B, while L_4 corresponds to Motors C and D). With the increase in L_3 and L_4, the cogging torque of Motors A and C both show a trend of initial increase, followed by a decrease, and subsequent continuous rise. The cogging torque of Motor A reaches a local minimum at $L_3 = 3.8$ mm, whereas that of Motor C reaches a local minimum at $L_4 = 37$ mm. The cogging torque of Motors B and D decreases with the increase in L_3 and L_4, respectively. When L_3 and L_4 have small values, although these two motors have high torque ripple and average torque, their cogging torque is also large under this condition. Therefore, Motors A and C were selected for subsequent comparative analysis.

At the local minimum of cogging torque for Motor A and Motor C, the average torque, cogging torque, and torque ripple of Motor A are 118.54 N·m, 174.26 mN·m, and 3.27%, respectively; the average torque, cogging torque, and torque ripple of Motor C are 117.71 N·m, 176.14 mN·m, and 3.15%, respectively.

In this paper, priority was given to the optimization of average torque, torque ripple, and cogging torque, while the cost issue was provided as a reference. Using N30, the cost could be reduced by approximately 30 RMB per kilogram. Since cost was not prioritized as an optimization objective in this study,

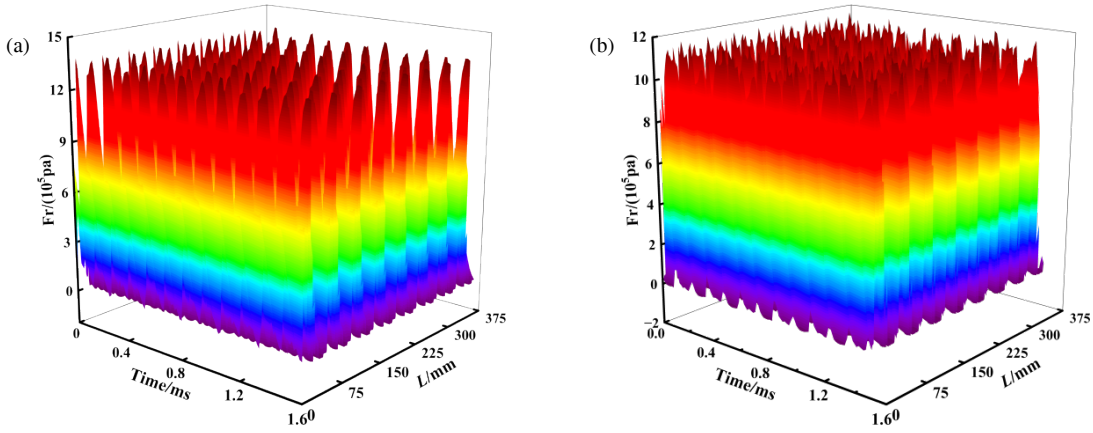

FIGURE 11. Three-dimensional radial electromagnetic force density waveforms: (a) Three-dimensional radial electromagnetic force density waveform before optimization, (b) Three-dimensional radial electromagnetic force density waveform after optimization.

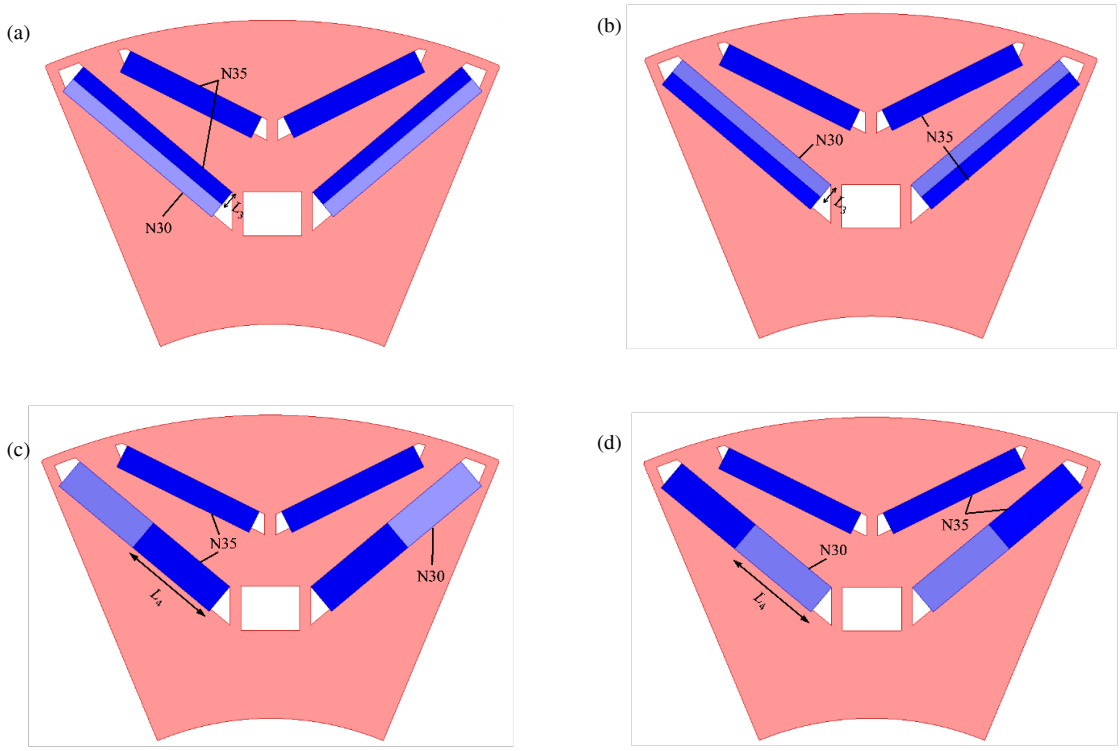

FIGURE 12. Rotor structures of four motors: (a) Rotor structure of Motor A, (b) Rotor structure of Motor B, (c) Rotor structure of Motor C, (d) Rotor structure of Motor D.

TABLE 5. Comparison of performance parameters for four configurations.

Performance Parameters	Motor A	Motor B	Motor C	Motor D
Average Torque (N·m)	116.91	116.83	116.94	116.83
Torque Ripple (%)	3.17	3.14	3.21	3.52
Cogging Torque (mN·m)	164.46	175.27	177.29	178.35
Core Loss (kW)	1.646	1.645	1.651	1.682

no quantitative analysis of the cost was performed. Based on a comprehensive consideration of the overall performance, the PM combination scheme of Motor A was adopted, and the optimal value of L_3 was determined to be 3.8 mm. Under this configuration, the motor achieved an average torque of 118.54 N·m, torque ripple of 3.27%, and cogging torque of 174.26 mN·m.

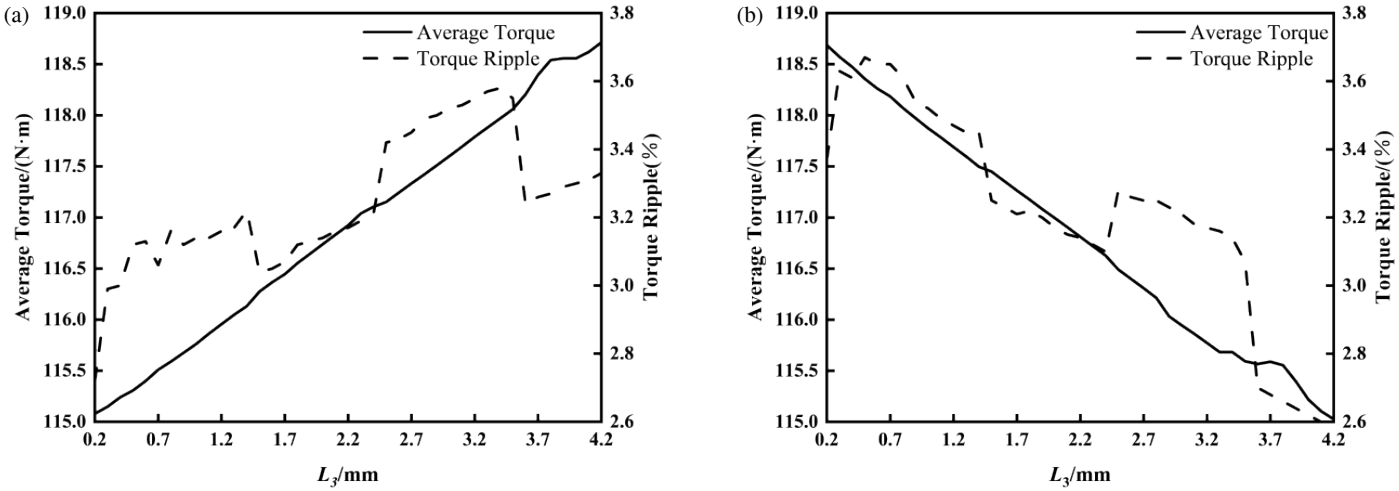

FIGURE 13. Influence curves of L_3 on the performance of Motors A and B: (a) Motor A, (b) Motor B.

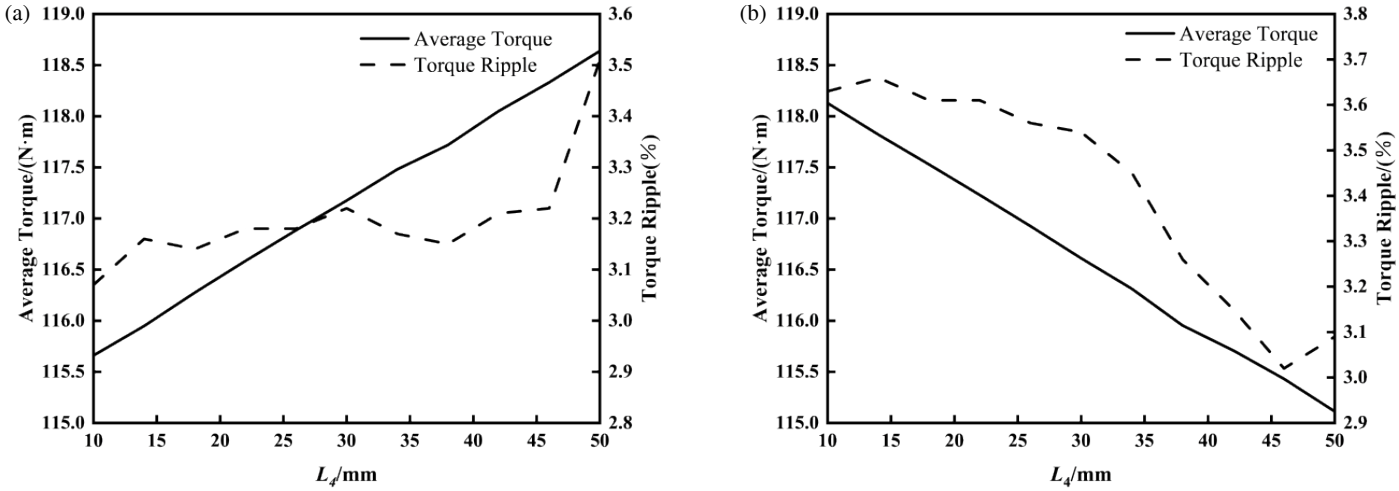

FIGURE 14. Influence curves of L_4 on the performance of Motors C and D: (a) Motor C, (b) Motor D.

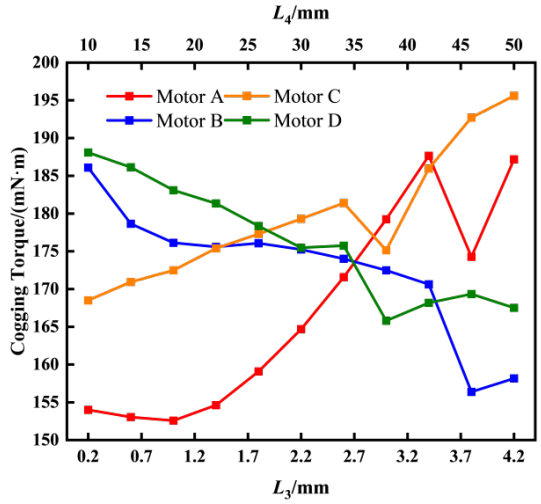

FIGURE 15. Influence curves of maximum cogging torque for four motors.

5. HALBACH MAGNETIZATION OPTIMIZATION

The motor designed in this study adopts a VV-type interior permanent magnet structure. Each magnet slot could accommodate multiple pre-magnetized segments, which were assembled manually or automatically. Compared with a single radially magnetized magnet block, this increased the manufacturing complexity, but it remained within the achievable range of advanced motor production lines. The magnetization process involved pre-magnetizing each segment individually before assembly. Because the first layer of the permanent magnets utilizes hybrid permanent magnets, Halbach magnetization optimization is applied to the second layer of permanent magnets. A parametric sweep was performed on the magnetization angle θ and length L_m to determine the most suitable magnetization angle and length. The Halbach magnetization configuration of the permanent magnets is illustrated in Fig. 16.

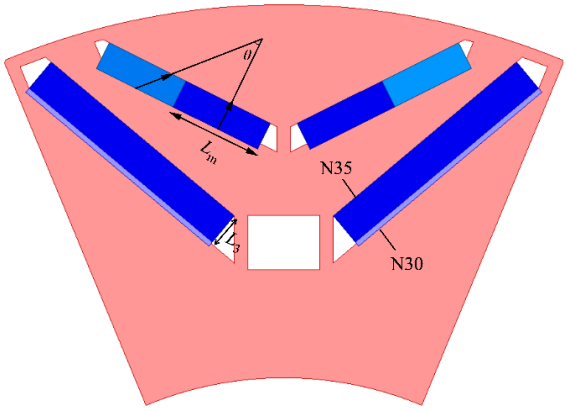

FIGURE 16. N-pole magnetization configuration of permanent magnets.

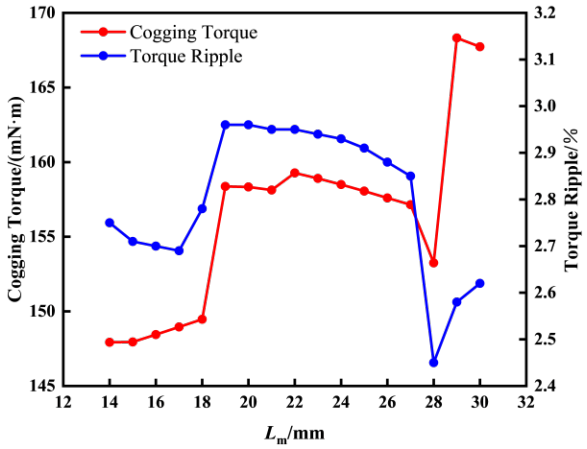

FIGURE 17. Influence of magnetizing length L_m on cogging torque and torque ripple.

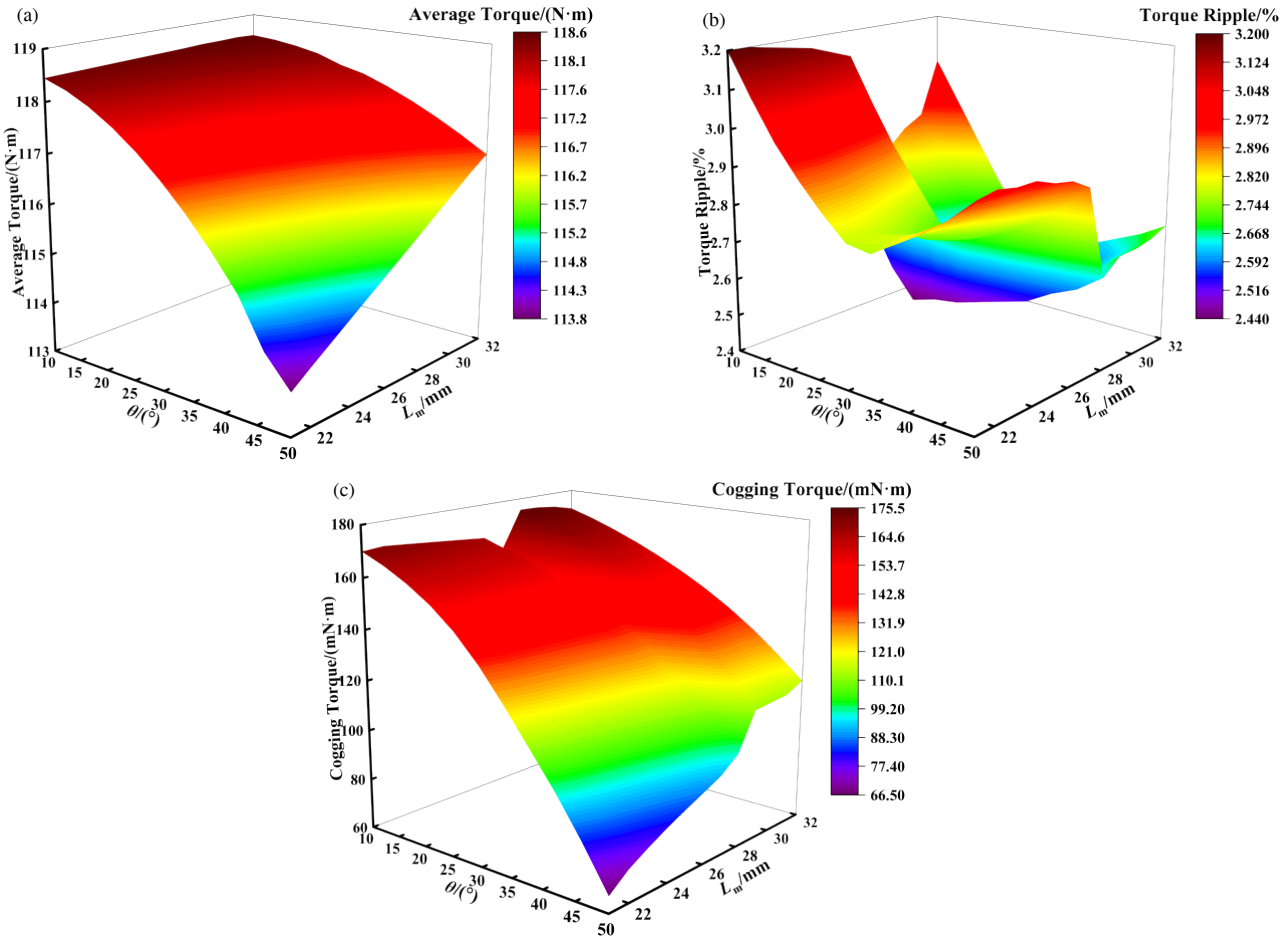

FIGURE 18. Response surface results for the magnetization angle and length: (a) Response surface of average torque, (b) Response surface of torque ripple, (c) Response surface of cogging torque.

5.1. Optimization of Permanent Magnet Magnetization Length Through Parametric Sweep

To investigate the influence of magnetization length L_m on torque ripple and cogging torque, the initial value of the magnetization angle θ was set to 20° for the ease of comparison. A parametric sweep was performed on magnetization length L_m to identify the optimal value that achieves both low cogging torque and low torque ripple. The sweep results are shown in Fig. 17.

As shown in Fig. 17, the torque ripple initially increased with the magnetization length, then decreased, and subsequently increased again, indicating the existence of a point where the

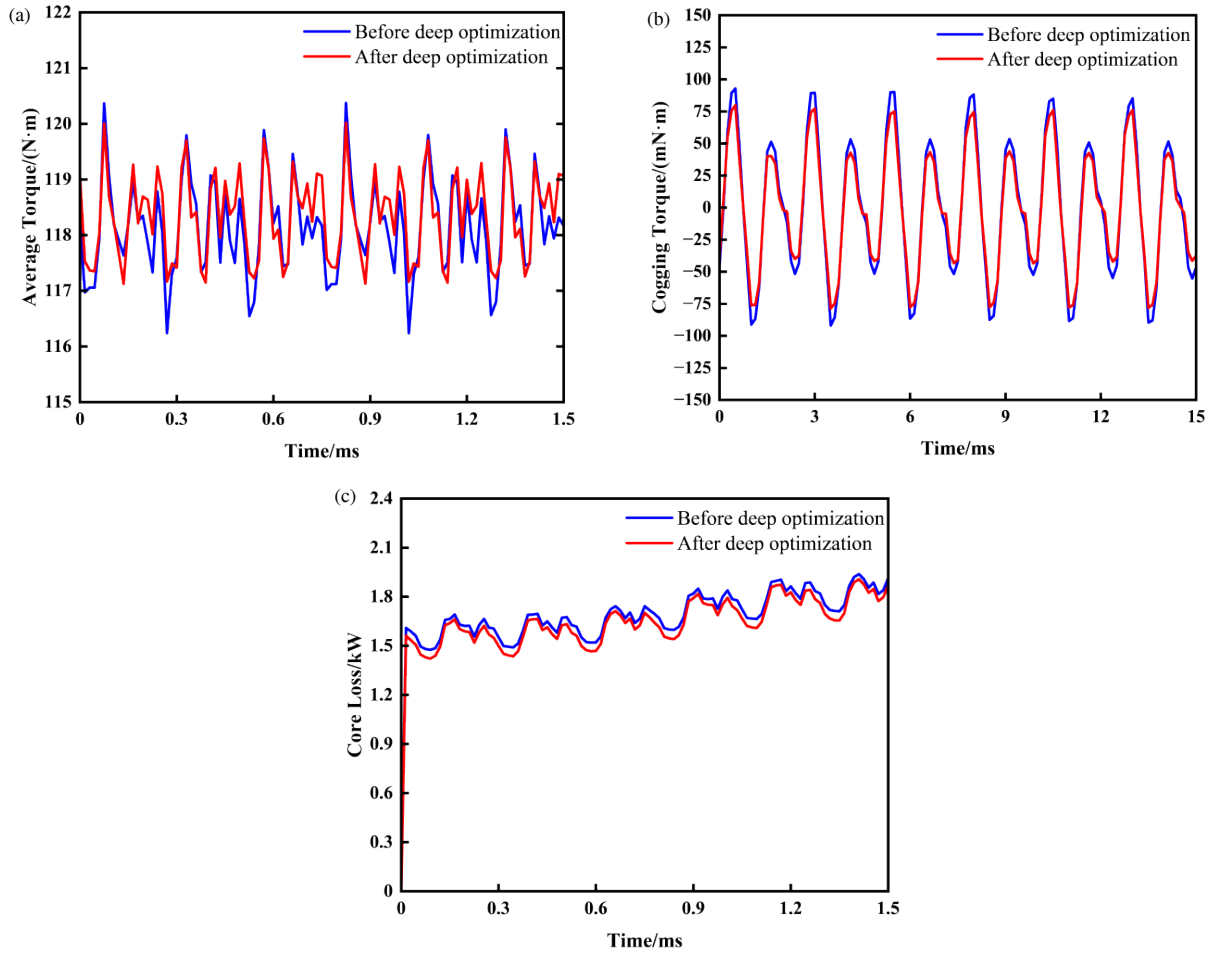

FIGURE 19. Comparison curves of various performance parameters after deep optimization: (a) Torque comparison curve, (b) Cogging torque comparison curve, (c) Core loss comparison curve.

TABLE 6. Variation range of magnetizing length and magnetizing angle.

Parameters	Variation Range
L_m (mm)	$21 \sim 32$
θ/(°)	$10 \sim 50$

torque ripple reaches a minimum value. The variation pattern of the cogging torque with magnetization length was consistent with that of the torque ripple. It can be observed that the magnetization length L_m has a significant effect on the reduction of both cogging torque and torque ripple. Therefore, it is necessary to consider the collaborative optimization of magnetization length L_m and magnetization angle θ.

5.2. Collaborative Optimization of Magnetization Angle and Length of Permanent Magnets

To determine better motor parameters, the magnetizing length was optimized parametrically, and the influence of the magnetizing angle was considered, keeping it within a certain range, as shown in Table 6.

The parametric sweep results for the average torque, torque ripple, and cogging torque are shown in Fig. 18.

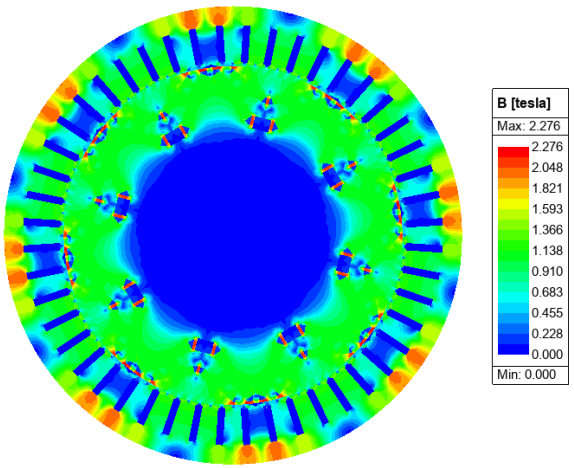

FIGURE 20. Magnetic flux density contour map of the motor.

As shown in Fig. 18(a), the average torque decreases with increasing magnetization angle and increases with increasing magnetization length. Fig. 18(b) presents the response surface of the torque ripple, where it can be observed that the torque ripple initially decreases and then increases with an increas-

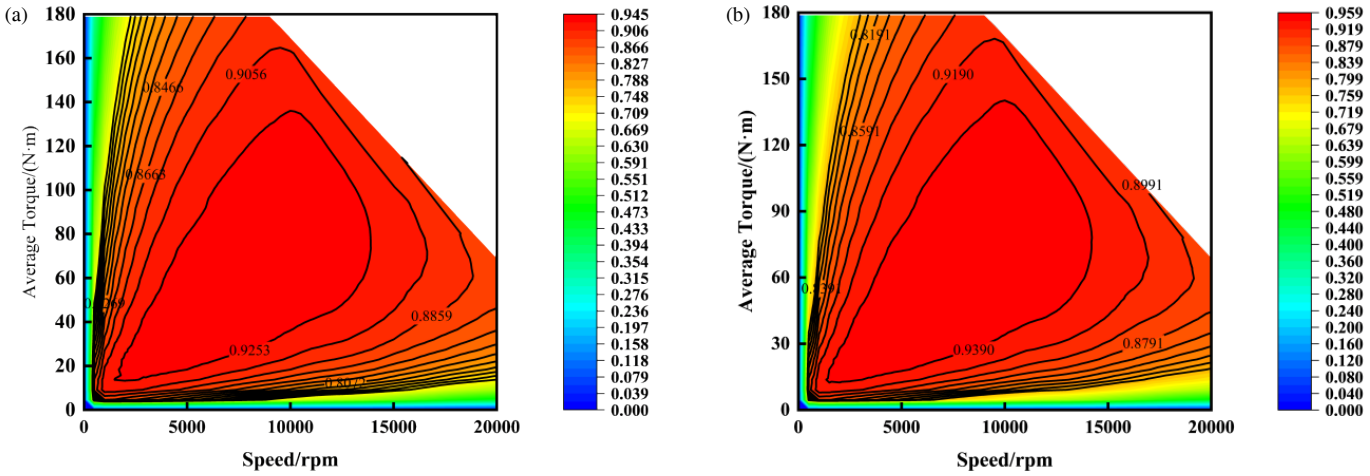

FIGURE 21. Motor efficiency map: (a) Before optimization. (b) After optimization.

TABLE 7. Comparison of motor performance parameters after deep optimization.

Parameters	Before Optimization	After Optimization
Average Torque (N·m)	118.25	118.33
Torque Ripple (%)	3.5	2.44
Cogging Torque (mN·m)	184.81	155.08
Core Loss (kW)	1.686	1.643

ing magnetization angle and length. Fig. 18(c) shows that the cogging torque decreases with increasing magnetization angle, while it exhibits a trend of initially increasing, then decreasing, and subsequently increasing again with an increase in the magnetization length.

Although increasing the magnetization angle significantly reduces the cogging torque, it also leads to a substantial decrease in the average torque, whereas the torque ripple remains at a relatively high level. Through a comprehensive comparison, it is more appropriate to select a scanning point near the minimum torque-ripple region, where the average torque is relatively high, and the cogging torque is maintained at a relatively low level. Therefore, the magnetization length $L_m = 28$ mm and magnetization angle $\theta = 18°$ were selected. At this operating point, the average torque was 118.33 N·m; the torque ripple was as low as 2.44%; and the cogging torque was reduced to 155.08 mN·m.

After deep optimization through measures such as permanent magnet structure adjustments and Halbach magnetization, the curves of the motor's average torque, cogging torque, and core loss are shown in Figs. 19(a)–(c), with the specific values listed in Table 7. It can be seen that after deep optimization, all performance parameters of the motor have been comprehensively improved. Notably, even with the use of N30 permanent magnets, which have a lower magnetic energy product, the average torque increased rather than decreased following deep optimization.

To compare the performance of the designed dual-V hairpin-winding interior permanent magnet synchronous motor with that of previous hairpin-winding interior permanent magnet synchronous motors, the hairpin-winding dual-layer V-shaped permanent magnet synchronous motor designed in [9] was taken as an example for investigation. Under the same 8-pole, 48-slot configuration and similar motor dimensions, the optimized motor in [9] achieves a maximum speed of only 12,000 r/min, a rated torque of only 82.9 N·m, and a cogging torque of 331.6 mN·m — far higher than that of the proposed motor (the parameters of the motor designed in this paper are shown in Table 7). Overall, the motor designed in this paper exhibits superior electromagnetic performance and satisfies the demands of high-performance new energy vehicle motors.

After the optimization of the permanent magnet material and Halbach magnetization, the combined diagram of the magnetic flux density cloud map and magnetic flux line distribution of the motor under no-load conditions is shown in Fig. 20. It can be observed that the magnetic flux density near the magnetic bridges is the most prominent, with a maximum value reaching 2.276 T. The flux density distribution is uniform and reasonable, indicating that the magnetic circuit design of the motor is appropriate and that the magnetic isolation capability of the flux barriers meets the requirements.

After optimizing the PM material and Halbach magnetization, a comparison of the motor efficiency maps is presented in Fig. 21. It can be seen from the figure that the motor efficiency is increased by approximately 1.4% over most of the speed range, and the efficiency of the optimized motor can reach more than 92% at the vast majority of operating speeds, which meets the design requirements of a wide operating range and high efficiency.

6. CONCLUSION

To address the trade-off between improving output torque and suppressing cogging torque and torque ripple in interior permanent magnet synchronous motors, this study proposes a multi-objective optimization design method that combines stator and rotor auxiliary slots, damping hole structures, and hybrid permanent magnets (N30 and N35). Through theoretical analysis, finite element simulation, parametric sweep, sensitivity analysis, and a multi-objective hierarchical optimization method, the key structural parameters of the motor were systematically optimized, and its electromagnetic performance, vibration, and noise characteristics were thoroughly investigated. The main conclusions are as follows.

1) After introducing a damping hole structure in the rotor, the average torque of the motor increased by 14.16 N·m, and the torque ripple was reduced by 1.86%. Therefore, auxiliary slots were opened on the stator and rotor cores, which effectively suppresses the cogging torque.

2) The key parameters were identified through a sensitivity analysis, and a multi-objective hierarchical optimization method was adopted to perform multi-objective optimization of the motor. The final optimized scheme achieved an average torque of 118.25 N·m while reducing the torque ripple to 3.4%.

3) A hybrid permanent magnet configuration combining N30 and N35 was adopted, and the arrangement was optimized through a parametric sweep. The results indicate that Configuration 1 (N35 in the upper layer and N30 in the lower layer) exhibits better performance in terms of torque ripple and cogging torque than the other configurations.

4) After optimization, the radial electromagnetic force amplitude of the motor was reduced from 1.33 to 0.98 MPa. The radial electromagnetic force density was significantly decreased in both the time and spatial domains.

5) Finally, through the collaborative optimization of the Halbach magnetization angle and length of the second-layer permanent magnets, the average torque was increased to 118.33 N·m; the torque ripple was reduced to as low as 2.44%; and the cogging torque was decreased to 155.08 mN·m.

ACKNOWLEDGEMENT

This work was supported by the Fund of Anhui Mining Machinery and Electrical Equipment Coordination Innovation Center (Anhui University of Science and Technology) under grant No. GJZZX2025KF01.

REFERENCES

[1] Chen, H., N. A. O. Demerdash, A. M. El-Refaie, Y. Guo, W. Hua, and C. H. T. Lee, "Investigation of a 3D-magnetic flux PMSM with high torque density for electric vehicles," *IEEE Transactions on Energy Conversion*, Vol. 37, No. 2, 1442–1454, 2022.

[2] Monadi, M., M. Nabipour, F. Akbari-Behbahani, and E. Pouresmaeil, "Speed control techniques for permanent magnet synchronous motors in electric vehicle applications toward sustainable energy mobility: A review," *IEEE Access*, Vol. 12, 119 615–119 632, 2024.

[3] Choi, G. and G. Bramerdorfer, "Comprehensive design and analysis of an interior permanent magnet synchronous machine for light-duty passenger EVs," *IEEE Access*, Vol. 10, 819–831, 2022.

[4] Sun, K. and S. Tian, "Multiobjective optimization of IPMSM with FSCW applying rotor notch design for torque performance improvement," *IEEE Transactions on Magnetics*, Vol. 58, No. 5, 1–9, 2022.

[5] Zou, T., D. Gerada, A. L. Rocca, M. Moslemin, A. Cairns, M. Cui, A. Bardalai, F. Zhang, and C. Gerada, "A comprehensive design guideline of hairpin windings for high power density electric vehicle traction motors," *IEEE Transactions on Transportation Electrification*, Vol. 8, No. 3, 3578–3593, 2022.

[6] Kim, J., C. Kim, Y.-D. Shim, and E.-H. Lee, "Investigation of plastic deformation and electromagnetic interaction for copper losses caused by hairpin motor manufacturing," *IEEE Transactions on Transportation Electrification*, Vol. 11, No. 4, 10 583–10 592, 2025.

[7] Jansson, E., T. Thiringer, and E. A. Grunditz, "Influence of flux barrier shape and mechanical constraints on field-weakening performance in double-layer interior permanent magnet machines," *IEEE Transactions on Energy Conversion*, Vol. 40, No. 1, 30–42, 2025.

[8] Dai, L., J. Gao, S. Niu, and S. Huang, "Multi-electromagnetic performance optimization of double-layer interior permanent magnet synchronous machine," *IEEE Transactions on Industrial Electronics*, Vol. 71, No. 11, 14 535–14 545, 2024.

[9] Xie, Y., H.-y. Li, W. Cai, and Z.-h. He, "Design and research of hairpin winding double-layer interior permanent magnet synchronous motor," *Electric Machines and Control*, Vol. 26, No. 4, 47–56, 2022.

[10] Zhou, H., X. Wang, W. Zhao, Z. Xing, and J. Liu, "Research on magnetic field prediction of synchronous reluctance motor considering structure of multilayer flux barrier and saturation of rotor core," *IEEE Transactions on Transportation Electrification*, Vol. 11, No. 2, 5983–5998, 2025.

[11] Liu, C., S. Zuo, X. Wu, B. Yin, H. Zhuang, and S. Wang, "Torque ripple reduction of permanent magnet-assisted synchronous reluctance motors based on equivalent slotting effect and auxiliary flux barriers," *IEEE Transactions on Transportation Electrification*, Vol. 11, No. 2, 7054–7065, 2025.

[12] Zhang, Y., Y. Yang, Z. Y. Gu, L. Li, and T. Ma, "Multi-objective optimization for noise reduction of IPMSM based on non-uniform air gap," *IEEE Access*, Vol. 12, 48 819–48 829, 2024.

[13] Han, J., Y. Sun, P. Zheng, H. Qi, J. Dong, Y. Liu, C. Zhang, B. Ge, and W. Li, "Influence of complex fluid flow on temperature distribution in the rotor region of large hydrogenerator under the rotor rotation," *IEEE Access*, Vol. 10, 3252–3262, 2022.

[14] Wan, X., S. Yang, Y. Li, Y. Shi, and J. Lou, "Minimization of cogging torque for V-type IPMSM by the asymmetric auxiliary slots on the rotor," *IEEE Access*, Vol. 10, 89 428–89 436, 2022.

[15] Huang, C., R. Jia, B. Chen, M. Zhang, H. Chen, Y. Wang, and J. Mao, "Research on cogging torque reduction based on multi-parameter optimization of auxiliary slots and pole-arc coefficient," *Journal of Electrical Engineering & Technology*, Vol. 20, No. 3, 1439–1449, 2025.

[16] Kazemisangdehi, S., Z. Q. Zhu, L. Chen, L. Yang, and Y. Zhou, "A mixed hybrid rare-earth and ferrite magnet asymmetric V-shape IPMSM," *IEEE Transactions on Transportation Electrification*, Vol. 11, No. 4, 8742–8755, 2025.

[17] Ajamloo, A. M., A. Ghaheri, M. N. Ibrahim, and P. Sergeant, "A new hybrid permanent magnet-assisted synchronous reluctance motor with efficient utilization of rare-earth permanent magnets," *IEEE Transactions on Energy Conversion*, Vol. 40, No. 2, 1325–1338, 2025.

[18] Diao, C., W. Zhao, L. Li, C. Liu, M. Tian, and X. Wang, "Analytical modeling and optimization of permanent magnet synchronous machine with hybrid magnets," *IEEE Transactions on Industry Applications*, Vol. 61, No. 1, 243–254, 2025.

[19] Xia, J., M. Qi, T. Dong, and M. Song, "Parameter sensitivity analysis and optimization of electromagnetic force waves of fractional slot surface-mounted PM motor with external rotor," *IEEE Access*, Vol. 11, 91 756–91 766, 2023.

[20] Gu, Y., X. Wang, P. Gao, and X. Li, "Mechanical parametric sensitivity analysis of high-speed permanent magnet synchronous machine," *IEEE Transactions on Applied Superconductivity*, Vol. 31, No. 8, 1–4, 2021.

[21] Xu, R. and W. Tong, "Multi-objective hierarchical optimization of interior permanent magnet synchronous machines based on rotor surface modification," *CES Transactions on Electrical Machines and Systems*, Vol. 6, No. 4, 352–358, 2022.

[22] Chu, J., H. Cheng, J. Sun, C. Peng, and Y. Hu, "Multi-objective optimization design of hybrid excitation double stator permanent magnet synchronous machine," *IEEE Transactions on Energy Conversion*, Vol. 38, No. 4, 2364–2375, 2023.

[23] Wu, Z., C. Song, and W. Deng, "Radial electromagnetic force and vibroacoustic mechanism analysis of integer slot permanent magnet synchronous motors," *IEEE Transactions on Transportation Electrification*, Vol. 11, No. 6, 13 568–13 578, 2025.

[24] Hong, J., L. Gui, and J. Cao, "Analysis and experimental verification of the tangential force effect on electromagnetic vibration of PM motor," *IEEE Transactions on Energy Conversion*, Vol. 38, No. 3, 1893–1902, 2023.

[25] Zhao, C., M. Cheng, Y. Wang, S. De, S. Shi, C. Song, and Z. Wang, "Analytical method of stator modal analysis for stator-permanent magnet machines," *IEEE Transactions on Transportation Electrification*, Vol. 11, No. 1, 2088–2096, 2025.

[26] Srikhumphun, P., P. Seangwong, J. Jongudomkarn, A. Siritaratiwat, N. Fernando, S. Somkun, and P. Khunkitti, "Design optimization and comparative study of skewed halbach-array magnets torus axial-flux permanent magnet motors for electric vehicles," *IEEE Access*, Vol. 12, 99 912–99 920, 2024.